PROCEEDINGS OF SPIE

SPIEDigitalLibrary.org/conference-proceedings-of-spie

Registration of microtomography images: challenges and approaches

Christine Tanner, Bert Müller, Griffin Rodgers

Christine Tanner, Bert Müller, Griffin Rodgers, "Registration of microtomography images: challenges and approaches," Proc. SPIE 12242, Developments in X-Ray Tomography XIV, 122420T (14 October 2022); doi: 10.1117/12.2633922

SPIE.

Event: SPIE Optical Engineering + Applications, 2022, San Diego, California, United States

Invited Paper

Registration of microtomography images: Challenges and approaches

Christine Tanner*, Bert Müller, and Griffin Rodgers

Biomaterials Science Center, Department of Biomedical Engineering, University of Basel, 4123 Allschwil, Switzerland;

Biomaterials Science Center, Department of Clinical Research, University Hospital Basel, 4031 Basel, Switzerland;

ABSTRACT

The quantification of appearance and geometrical changes between structures captured across several images relies on the determination of correspondences between these image structures. Automatic methods for establishing sparse and dense spatial correspondences are feature tracking and image registration, respectively. Main registration challenges are weak image features, complex appearance change, large shape changes, and huge images. These challenges can make the problem intractable. We present approaches to overcome these challenges for registration tasks including microtomography images. Applications include assessing tissue changes due to embedding material, comparison of microtomography with optical microscopy images, and optimization of process parameters for materials.

Keywords: Image registration, X-ray virtual histology, synchrotron radiation, hard X-ray microtomography, volumetric imaging

1. INTRODUCTION

Image registration is the method to determine dense spatial correspondences between two or more images. It is required whenever images or image regions need to be compared in detail. Image registration applications include quantification of volume and shape changes, fusion of information from several image modalities and/or multiple tissue states, motion quantification, detection of patterns, and segmentation propagation by registration. Here we describe our experiences with registration of micro computed tomography (μCT) images, which can pose the additional challenges of huge image sizes and limited soft-tissue contrast.[1]

Regularization optimization. Tissue deformations require transformation models with many degrees of freedom (DOFs) to be locally adaptive.[2] The selected image similarity measure will improve for registrations with more DOFs thanks to the increased number of free parameters and hence image similarity cannot be employed as an evaluation measure.[3–5] It is very important to have realistic transformations, as these act as interpolation functions when no evidence from the image exist, e.g. in homogeneous image regions. We have compared two approaches for this trade-off namely regularization versus reduction of degrees of freedom, and determined in an unsupervised way the more suitable approach and amount of regularization.[6]

Distributed multi-resolution approach. μCT images are often very large in size, e.g. to cover a mouse brain with an isotropic voxel resolution of 0.65 μm an image of size of approximately 15,000 $\times$ 15,000 $\times$ 14,800 voxels = 3.3 teravoxels is required, i.e. a file size of 6.6 TB for 16 bits encoding. Registration of such huge images often leads to problems, as the images and their spatial transformation exceed memory limits and/or cause excessive runtimes. We therefore developing a distributed multi-resolution approach, in the spirit of image and transformation multi-resolution pyramids, where registrations of large image regions are distributed to independent tasks to avoid violating memory limitations. Challenges of such a distributed multi-resolution registration approach include keeping track of regions, composing transformations from coarse to fine resolutions, and fusing local results.

*Send correspondence to C.T., e-mail: christine.tanner@unibas.ch, Telephone: +41 61 207 54 34, www.bmc.unibas.ch

Developments in X-Ray Tomography XIV, edited by Bert Müller, Ge Wang, Proc. of SPIE Vol. 12242, 122420T
 · 0277-786X · doi: 10.1117/12.2633922

Multi-modal image registration. Very useful information can be gained by combining the information from different image modalities as these modalities probe various properties of the tissue, e.g. density from μCT, water content from T1-weighted Magnetic Resonance Imaging (MRI), water diffusion from diffusion-weighted MRI, tracer uptake from Positron Emission Tomography (PET), and function information from histological stains. Such fused multi-spectral images do improve differentiation of tissue types.[7] Yet this requires determining accurate spatial correspondence, which is difficult as the appearance of the images is vastly dissimilar and hence image similarity measures are hard to devise. Learning these similarities requires a suitable training data of dense correspondences,[8,9] which realistically can only be provided by simultaneous image acquisitions and simulations of realistic transformations. Feature-based registration approaches often suffer from nonlinear intensity variations[9] and provide for the investigated sample in initial tests unsatisfactory results.[10] Instead, we employed manually determined correspondences of landmarks for guiding the intensity-based deformable registration.

Missing correspondences. Quantification of material removal or addition via image registration has the issue of missing correspondences. Hence it is important to be able to define the image region which is present in both images, such that image registration is only optimized for the selected region.

2. MATERIALS AND METHODS

2.1 Materials

Mouse brains. The mouse brain stems from an experiment with approval of the veterinary office of the Canton of Zurich (license number ZH067/17). After death, the brain was extracted from a seven-month-old male C57BL/6J mouse (Janvier Labs, Le Genest-Saint-Isle, France) and fixed by immersion in 4% formaldehyde solution (Sigma Aldrich, Darmstadt, Germany) and subsequently immersed in 50%, 70%, 80%, 90%, and 100% ethanol solutions and xylene for two hours each (Carl Roth GmbH, Karlsruhe, Germany).[2]

Rat jaw. This work includes images after stem cell-mediated distraction of the right half jaw of Rat 1, see Rodgers et al.[7] Images of the jaw in formalin and paraffin were acquired before and after its decalcification, respectively.

Aligners. The upper jaw of a subject was scanned with the intraoral scanner Medit i500 (Medit Corp., Seoul, South Korea), a 3D surface model was created from the interoral scan, and eight copies of the model were printed using the stereolithographic printer Formlabs Form3 (Formlabs, Somerville, Massachusetts). Eight NaturAligners® were thermoformed on the dental models with a pressure molding device (Biostar, Scheu-Dental, Iserlohn, Germany) at temperatures ranging from 112 °C to 201 °C and for foil thicknesses of 500 and 750 μm.[11]

Teeth. Sixteen not worth preserving teeth were extracted during clinical interventions, cleaned with an ultrasonic hand piece and freed from soft-tissue. Each tooth showed one to three independent caries lesions, resulting in a total of 23 lesions, which were manually removed following the principles of tooth preparation.[12]

2.2 Image Acquisition

Mouse brains. Hard X-ray microtomography was performed at the ANATOMIX beamline (Synchrotron SOLEIL, Gif-sur-Yvette, France).[13] An undulator gap of 10.3 mm and a 20 μm Au filter were selected to create a polychromatic beam with mean energy around 22 keV. Radiographs were recorded on a detector consisting of a 300 μm LuAG scintillator coupled to a scientific CMOS camera (Hamamatsu Orca Flash 4.0 V2, 2048 $\times$ 2048 pixels, 6.5 μm physical pixel size) by two photo objectives in tandem geometry (Hasselblad HC 4/210 and HC 2.2/100, 0.22 numerical aperture).[14] The resulting magnification factor was 2.1, yielding an effective pixel size of 3.1 μm.

For tomographic imaging, 5,900 projections were acquired with continuous 360° rotation about an off-center axis to nearly double the detector field-of-view. The exposure time was 50 ms and a single scan took seven

minutes. The field-of-view was extended vertically to image the entire brain by stitching together three to four height steps.

Tomographic reconstruction was done in `Matlab` (The MathWorks, Inc., Natick, USA) using the filtered backprojection algorithm with the standard Ram-Lak filter. To reduce noise at the expense of spatial resolution, a Gaussian filter with $\sigma = 1.25$ pixels was applied to the unbinned data.[15] To reduce dataset size, another reconstruction was done with projections binned by a factor of 3 prior to reconstruction, i.e. with effective pixel size of 9.3 μm.

Rat jaw. Before decalcification, the rat jaw sample was imaged with a phoenix nanotom m (GE Sensing & Inspection Technologies GmbH, Wunstorf, Germany) laboratory microtomography systen. An acceleration voltage of 100 kV_p and a beam current of 100 μA were selected. Tomographic acquisition consisted of 2,000 equiangular projections around 360° rotation with an exposure time of 0.5 seconds per frame. Total acquisition time was about 100 minutes. An effective pixel size of 6.9 μm was selected to allow for imaging of the entire sample. Projections were binned by a factor of four and tomograms were reconstructed using the software phoenix datos|x (GE Sensing & Inspection Technologies GmbH, Wunstorf, Germany). The reconstruction software used a modified Feldkamp algorithm and provided ring-artefact and beam-hardening corrections. The resulting reconstruction had an effective pixel size of 27.6 μm.

The decalcified rat jaw was imaged at the beamline BW 2 (HASYLAB at DESY, Hamburg, Germany).[16] Absorption contrast mode was used at a photon energy of 14 keV. Tomography was done with an off-set rotation axis to fit the full sample within the field-of-view. A magnification of 1.76 was used, providing an effective pixel size of 5.2 μm and a spatial resolution of 9.4 μm. Tomographic imaging consisted of 1,440 equally spaced projections around 360° of rotation. Before reconstruction with a filtered back-projection, projections were binned by a factor of two to increase signal-to-noise ratio.[17] Reconstructed volumes were also binned by a factor of two to reduce image size, thus the final pixel size was 20.6 μm.

After tomographic imaging, the rat jaws were sliced along the horizontal plane into sections using a microtome Leica SM2010R (Leica Instruments GmbH, Nussloch, Germany). This slicing plane was selected because it contained both osteotomy sites and the complete distraction gap zone. Paraffin-embedded sections had a thickness of 2 μm and were stained with Hematoxylin and Eosin (H&E). Histology slides were imaged at 20× magnification using a plan-apochromatic objective using a Panoramic MIDI (3DHistech Ltd., Budapest, Hungary) slide scanner.

Aligners. We acquired two sets of tomographic data per aligner, namely the aligner mounted on the model (model + aligner) and the model without an aligner (model). Tomographic data acquisition was performed with nanotom m (phoenix—x-ray, GE Sensing & Inspection Technologies GmbH, Wunstorf, Germany), equipped with a nanofocus tube. We employed an acceleration voltage of 90 kV_p and a beam current of 200 μA. The effective pixel length of the radiographs was set to 33 μm and resulted in (33 μm)^3 voxels. The mean photon energy was increased by implementing a 0.5-mm-thick aluminum film behind the transmission target. A set of 2,000 radiographs was taken along 360 deg with an exposure time of 2 seconds per projection.

Teeth. For the analysis of caries removal and fillings, a total of 16 teeth were imaged. Each tooth was scanned three times, i.e. before treatment, after caries removal and after filling, using the SkyScan 1275 (Bruker, Belgium) commercial μCT system. Depending on tooth size, acceleration voltages between 60-75 kV_p, beam currents of 133-166 μA, and pixel sizes between 9 and 13 μm were selected. Either aluminium or bronze filters were used to limit beam hardening artefacts. Scan times varied between 15 minutes and nearly 7 hours, as differing exposure times from 75 to 4000 ms and number of frames to average from 4 to 9 were needed to provide satisfactory signal-to-noise ratio.

Reconstruction, ring artefact removal, and beam hardening correction were performed using the SkyScan `NRecon` software package (Version 1.7.4, Bruker, Kontich, Belgium).

2.3 Image Registration

We have used the open source registration software `elastix`[18,19] (version 5.0) extensively, as it is easy to install and run, is well-documented with online resources, and runs relatively fast, even for GB-sized images with complex transformation models. In addition to the standard registration functionalities, it also has useful features such as definition of image regions to be registered and the incorporation of landmark correspondences in the optimization function.

Regularization optimization. The process of fixation and embedding of tissue for histological analysis changes the tissue properties. The effects of such a process, from formalin fixation to paraffin embedding via a ascending alcohol series, were captured and analyzed for a mouse brain with μCT by Rodgers et al.[2,6,20,21] As local volume and intensity changes are expected, we employed a deformable transformation model, namely a grid of displacements vectors interpolated by B-Splines,[22] and mutual information (MI)[23–25] as image similarity measure. Alignment was optimized within the brain region using a mask to ignore surrounding media and sample container.[20,21] Regularization can be performed by reducing the number of grid points or by introducing a penalty term into the optimization function. We investigated the amount and type of regularization based on L-curve optimization[26] and Pareto efficiency.[20]

Registration of huge images. We are developing a distributed multi-resolution registration approach to cope with huge images. In the case of microtomography, these may come from mosaic-styled extended field-of-view acquisitions, which often result in teravoxel-sized datasets.[27–29] First, images are downsampled to a size such that they and the required transformation files fit into memory during image registration. Image registration is then performed for these low-resolution images. The resulting transformation provides the corresponding coordinates in the moving space, which can be used to define corresponding local regions, see Fig. 1 top. Region of interest in the high-resolution images can then be transformed based on the low-resolution registration result and/or independently registered if the degree of downsampling precludes accurate registration of fine structures, as illustrated in Fig. 1 bottom.

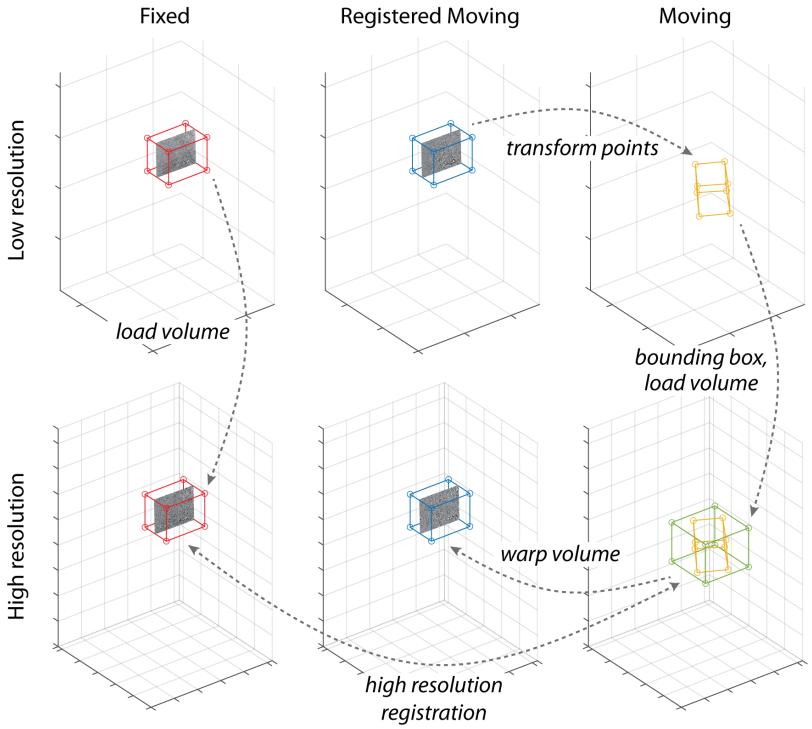

Figure 1. Illustration of framework for distributed multi-resolution image registration or transformation. (top) Registration is performed with downsampled images to fit in available memory. Given a local region in fixed space (red box, blue box), the resulting transformation provides the corresponding coordinates in moving space (yellow box). (bottom) Registration in high resolution space is then preformed between the red box and the green box enclosing the yellow box, as the transformed coordinates in the moving space can cover a skewed region with respect to the grid of the moving image.

Multi-modal image registration. We employed manually selected pairs of landmark to guide multi-modal image registration to study bone regrowth patterns.[7] For 3D-3D registration of μCT images a rat jaw before and after decalcification, we optimized non-rigid image registration with respect to maximizing normalized cross correlation and minimizing the distance between 50 landmark pairs within the `elastix` framework (version 4.9). For registration of the 2D histology image to the 3D μCT image of a decalcified rat jaw, we used 50 landmark pairs to find the corresponding deformed slice in the 3D image via rigid and affine image registration, and a thin-plate spline fit.[10] Final non-rigid registration of the extracted μCT slice was performed via `elastix` optimizing only for mutual information, i.e. without considering the landmarks.

Missing correspondences - Aligners. We performed an analysis of the thickness of NaturAligners® with 550 μm (NA.550) or 750 μm (NA.750) initial foil thickness and four temperatures during the thermoforming process.[11] The segmentation of the aligner required image registration, as the aligner and the model had very similar densities and hence μCT image intensities. This could not be avoided, as neither the 3D printing material for the model nor the NaturAligners® itself were allowed to be substantially changed to make the densities dissimilar. To avoid finding false correspondences between the dental model and aligner, we restricted the rigid registration to the bottom region of the model.

Missing correspondences - Teeth. The amount of remaining caries was analyzed after mechanical removal by μCT images for 16 extracted teeth to provide feedback on the manual treatment.[12] We registered the three states of each tooth, i.e. before caries removal, after caries removal, and after filling, in order to determine the amount of removed and filled material, and to enable visual inspection of the rim region within the context of its surrounding tissue. After manual pre-alignment with ITK-SNAP[30] (version 3.8.0), we automatically rigidly registered the tooth states with `elastix` by optimizing normalized correlation coefficient within the common region, i.e. after caries removal, to avoid mismatches to the removed or filled tissue.

3. RESULTS AND DISCUSSION

Regularization optimization. We tested bending energy penalty weights λ from 0 to 562 (at a grid spacing of 12 pixels) and grid spacings from 12 to 48 pixels (at $\lambda = 0$) to determine the amount and type of regularization. Plotting the resulting bending energy values versus the image dissimilarity measure (-MI), both min-max normalized, one gets a L-shaped curve[26] with the optimum at position [0 0], i.e. at the maximum mutual information and minimum bending energy, see Fig. 2. Fitting an exponential decaying function, one can observe that the optimum regularization is close to $\lambda = 46$, and that using a penalty on bending energy provides improved image similarity over reducing grid spacing, i.e. is Pareto efficient. Fig. 3 shows that little regularization, i.e. $\lambda = 0$, creates unrealistic volumetric strain patterns, while not improving image alignment.

While the optimal value for the regularization parameter is problem-specific, improving image similarity without introducing unnecessary deformations is a general trade-off in image registration. Controlling this trade-off via a regularization term instead of only reducing grid spacing has the advantage of greater local flexibility, i.e. larger deformations are possible locally if they improve image similarity considerably.

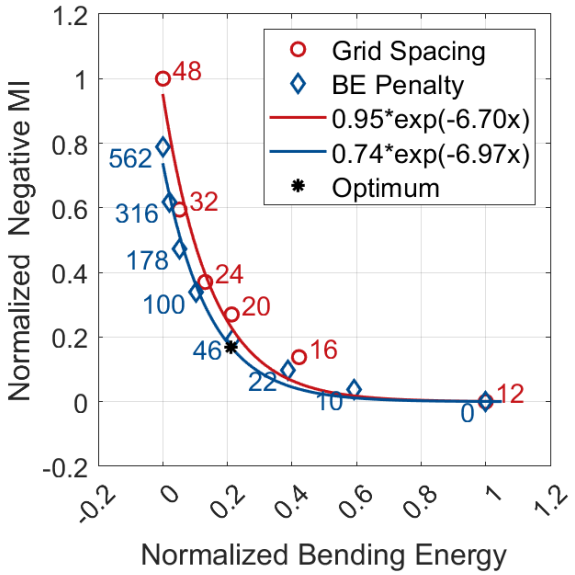

Figure 2. Unsupervised optimization of regularization via L-curve. Fitting an exponential decaying function to results of bending energy (BE) versus image dissimilarity negative mutual information (MI), both min-max normalized, for various grid spacings (12 to 48 pixels, $\lambda = 0$, red circles) and bending energy penalties (λ from 0 to 562, 12 pixels grid spacing, blue diamonds), one can determine the optimal regularization (closest point to [0 0], black star).

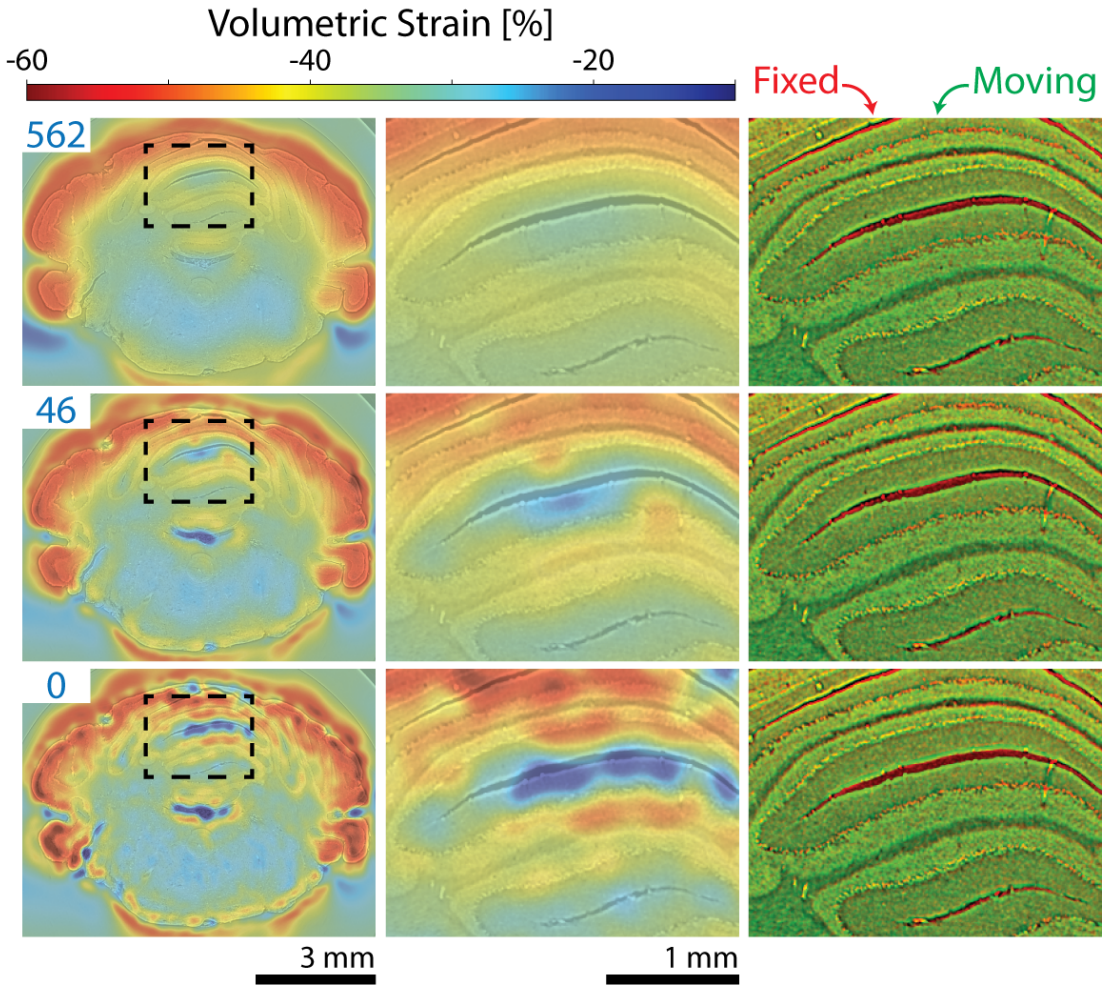

Figure 3. Illustration of volumetric strain and alignment for region with most improved mutual information with respect to highest regularization ($\lambda = 562$) after registration of xylene-embedded to formalin-fixated mouse brain.

Registration of huge images. For the mouse brain, an image resolution of 3.1 μm and a B-Spline transformation model with finest resolution of 12 pixels, images required 3× binning to fit into memory. We used the distributed multi-resolution registration approach to warp full-resolution, i.e. unbinned, image regions with the low resolution registration result to enable comparison of fine structures,[6] see Fig. 4. Note that these sub-regions can be additionally registered if necessary to achieve satisfactory correspondence of fine structures such as individual cells.

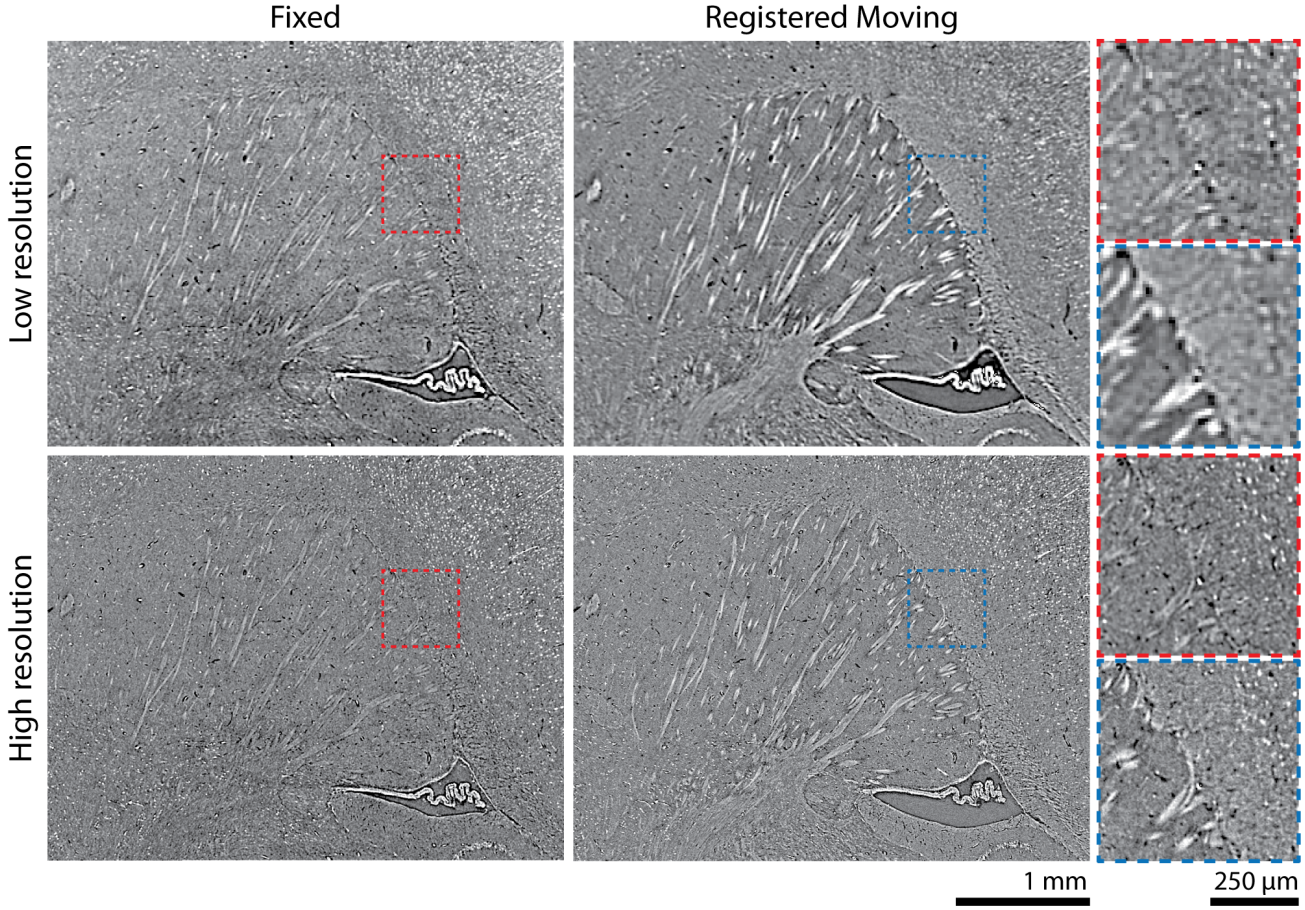

Figure 4. (top) Illustration of non-rigid alignment between (left) formalin-fixed and (right) ethanol-dehydrated mouse brain after registering the full images downsampled to 9.3 μm pixel resolution. (bottom) Applying the low resolution registration result to regions of the 3.1 μm images allows comparison of finer structures.

Multi-modal image registration We studied bone regrowth patterns in the jaw of a rat via μCT and histology imaging.[7] μCT images were acquired before and after decalcification of the jaw. Image appearance changed dramatically, with μCT images before decalcification showing only bones, while after decalcification soft-tissue becomes visible, see Fig. 5. Purely intensity-based image registrations failed due to this large appearance change. We therefore optimized the registration to stay close to the manually determined corresponding landmark pairs, while also improving image similarity (normalized cross-correlation).

Landmarks were also employed for extracting the deformed μCT slice corresponding to histology slice and perform a rigid and affine alignment. The final non-rigid alignment was purely intensity based. Fig. 6 top shows that the landmark distances reduce as expected for the rigid and affine registration, but also slightly for the final affine + non-rigid registration where they were not used. The improved alignment of the histology contours with the μCT features with progression of registration can be seen in the middle and bottom row. Registration of these three modalities enabled visual comparison and fusion of image information.[7]

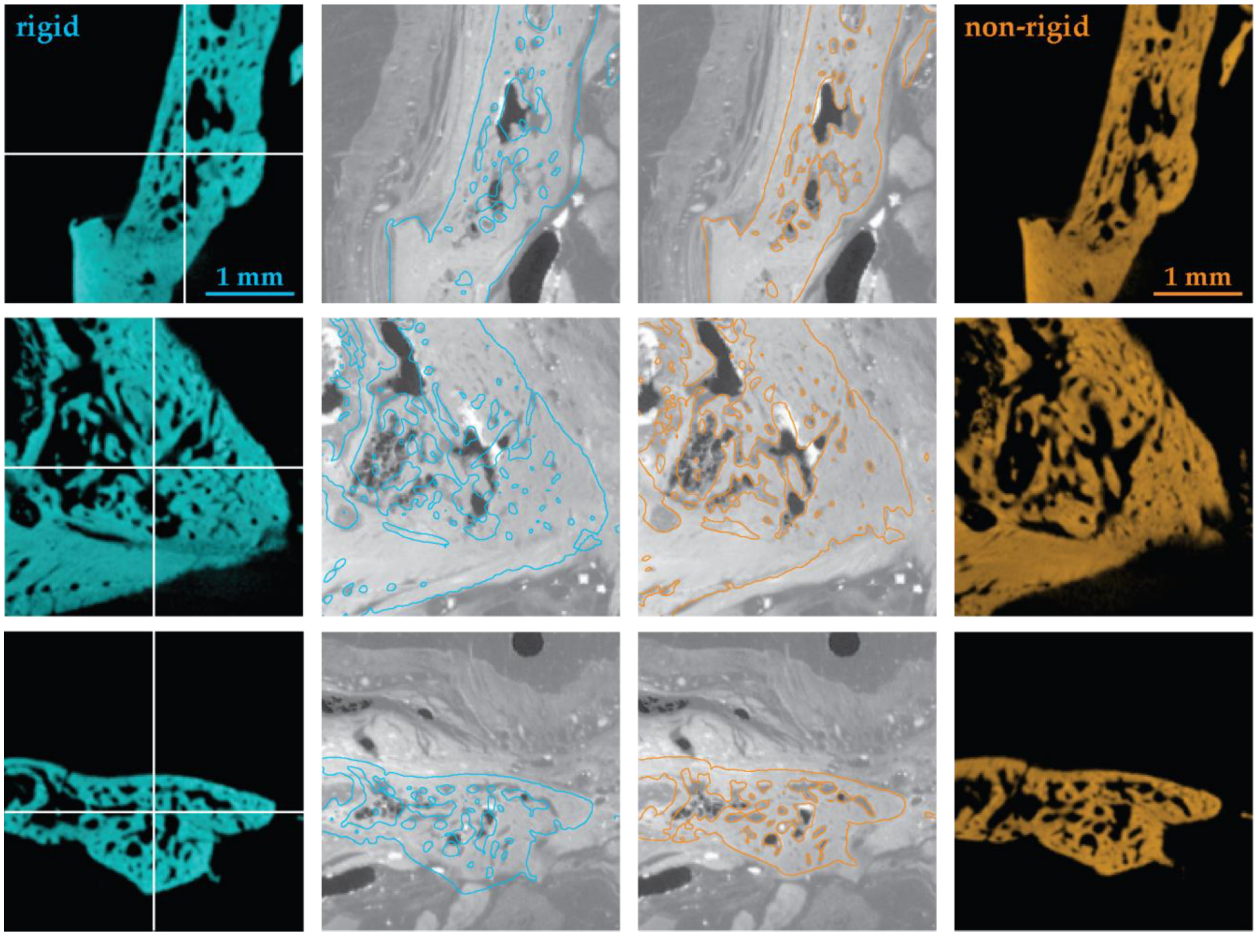

Figure 5. (Left) Rigid and (right) non-rigid registration results of images from rat jaw before decalcification (outer columns) and after decalcification (middle columns) from Rodgers et al.[7]

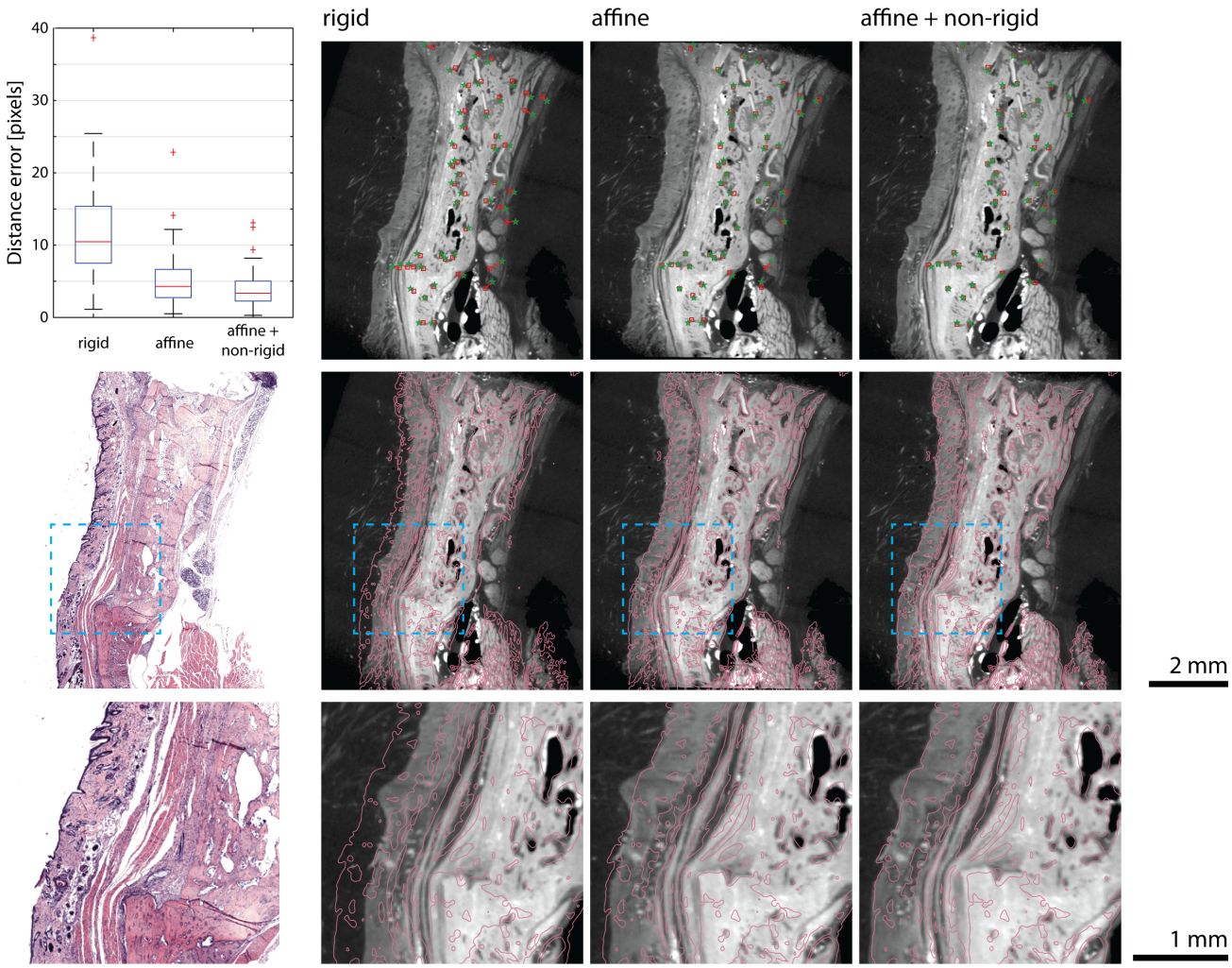

Figure 6. Multimodal image registration of 3D μCT image and 2D histology slice. (top) Distance error distribution and location of corresponding landmark pairs (green histology, red μCT). (middle, bottom) Alignment between histology image (left, contour) and μCT image after rigid, affine and affine+non-rigid registration.

Missing correspondences - Aligners. We registered the model to the model+aligner μCT images to segment the aligner, as model and aligner had very similar densities and hence image appearance, see Fig. 7(a). To avoid that the model was inadvertently registered with the aligner, we restricted the rigid registration to the bottom region of the model, see example overlay in Fig. 7(b). Taking the difference image after registration allows segmentation of the aligner and subsequent analysis of its thickness, see Fig. 7(c).

Missing correspondences - Teeth. Fig. 8 shows the results from rigidly registering a molar (tooth number 28) before and after removal of caries, and after filling. The difference images clearly show that the removed or filled tissue can be well discriminated. This allows automatic quantification of the removed or filled tissue volume and supports visual inspection of the rim region within the context of the removed tissue. Thresholding the difference image via Otsu's method[31] and keeping the largest connected component provides a volume of 9.0 mm^3 and 9.1 mm^3 for the removed and filled material, respectively. As determined by sparse manual segmentation, which was automatically shape interpolated,[32] the remaining caries is 2.7 % with respect to the rim region for this lesion. In contrast, the median value of remaining caries for all 23 lesions is 0.9%.

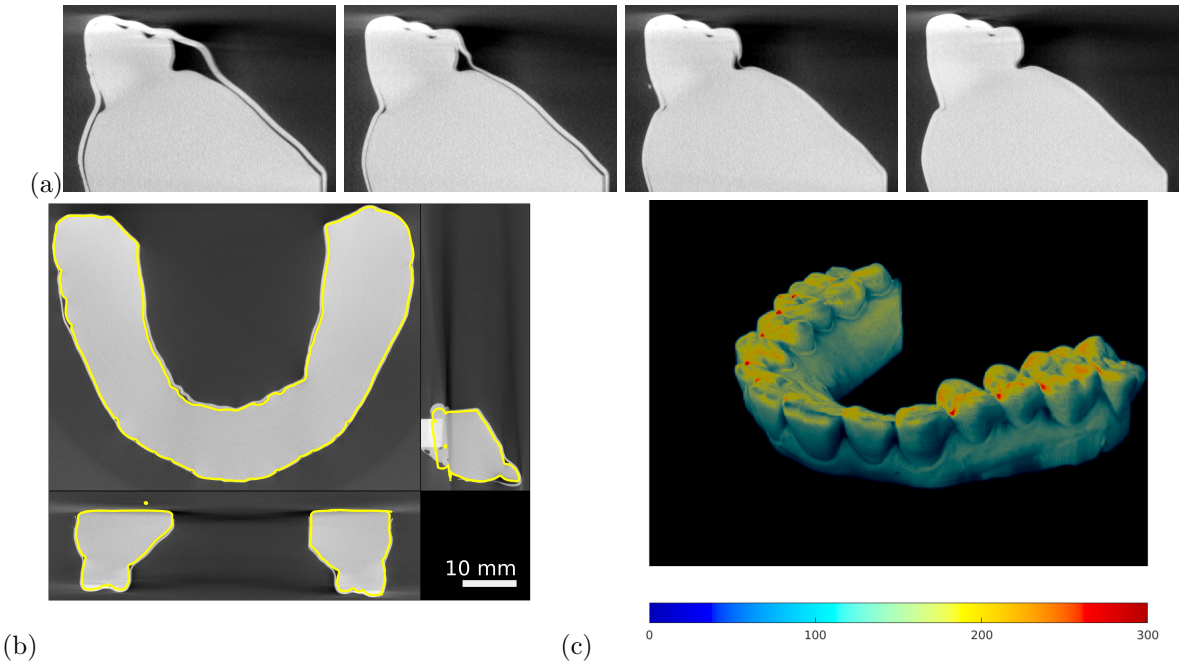

Figure 7. Thickness analysis for NaturAligners® with initial foil thickness of 550 μm. (a) Sagittal cut through model + aligner for processing temperatures (left→right) 112 °C, 142 °C, 173 °C and 200 °C. (b) Orthogonal slices after registration of model (yellow contours) to model + aligner (image) for 112 °C to enable segmentation of aligner. (c) Color-coded thickness in μm of aligner with processing temperature 200 °C.

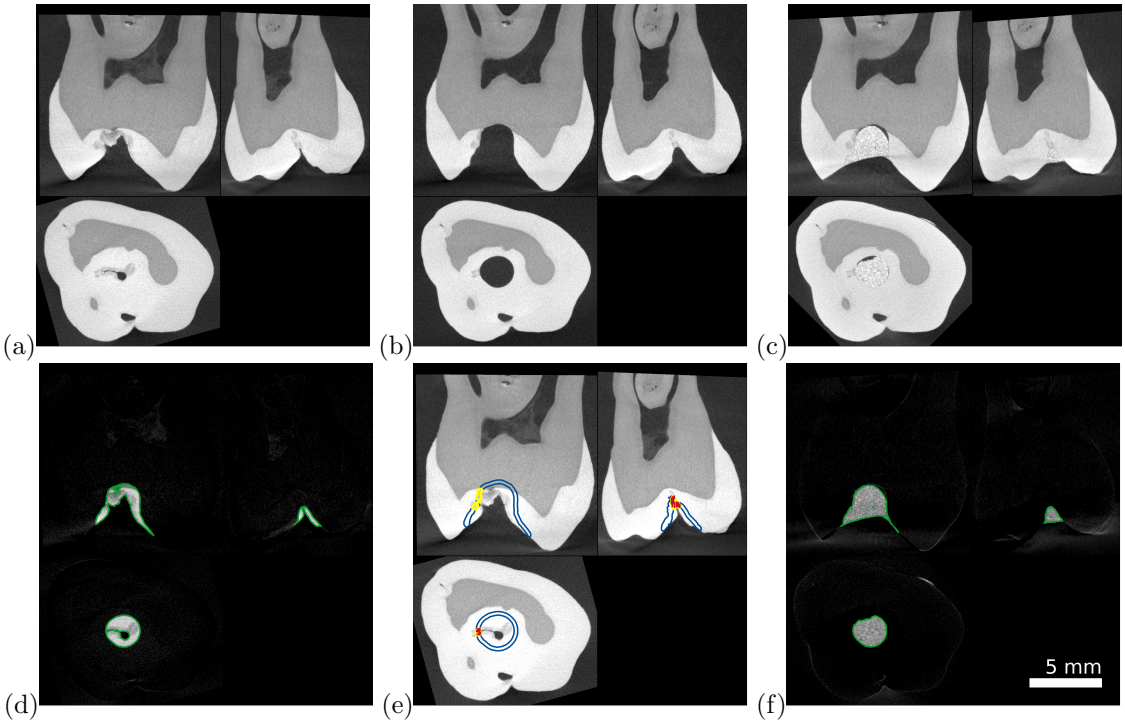

Figure 8. Orthogonal virtual cuts of registered tooth (a) before treatment, (b) after caries removal, and (c) after filling. Registration allows (d,f) automatic quantification of removed and filled tissue volumes (green contours) and (e) determining rim region (blue contours) within the context of the removed tissue for sparse manual segmentation of remaining caries (red contours), which was automatically interpolated (yellow contours).

4. CONCLUSION

Quantifying change between images or combining information from several images requires establishing dense spatial correspondences between the images, i.e. image registration. In this work, we reported how we overcome various challenges when registering μCT images for several applications. Few datasets with missing dense ground truth transformations and changing applications prohibit exploiting deep learning methods. Instead we successfully relied on analyzing the problem and devising a suitable approach. These included exploiting L-curve optimization and Pareto efficiency to determine the amount and type of regularization, developing a distributed multi-resolution registration framework, incorporation of manually determined landmarks where needed, and optimizing registration only with respect to the region present in both images.

Progress for accurate fully automatic multi-modal deformable image registration will rely on building a dedicated databases of well registered images to learn the relationship between image modalities for healthy and abnormal structures. Semi-automatic registration approaches, as presented in the work, will support creating such valuable datasets.

5. ACKNOWLEDGMENTS

We are grateful for financial support from the Swiss National Science Foundation (Project No. 185058) and the French National Research Agency (EQUIPEX project *NanoimagesX*, grant no. ANR-11-EQPX-0031), and from the Swiss National Science Foundation within the Micro- and Nanotomography project (Grant No. 133802). We are grateful for beamtime access at the Synchrotron SOLEIL, ANATOMIX beamline (experiment no. 20200712). Beamtime at DESY (Hamburg, Germany) was granted through the project proposals I-20110780 EC and I-20110555 EC.

We greatly appreciated the support from our colleagues Georg Schulz for image acquisition, Guido R. Sigron for annotation of manual landmarks, Rémi Ammann for the preparation of the NaturAligners® and manual determination of aligner thickness for validation of the automatic method, and Andrés Izquierdo for teeth treatment and manual segmentation of the residual caries.

REFERENCES

[1] Müller, B., Deyhle, H., Lang, S., Schulz, G., Bormann, T., Fierz, F. C., and Hieber, S. E., "Three-dimensional registration of tomography data for quantification in biomaterials science," *Int. J. Mater. Res.* **103**(2), 242–249 (2012).

[2] Rodgers, G., Kuo, W., Schulz, G., Scheel, M., Migga, A., Bikis, C., Tanner, C., Kurtcuoglu, V., Weitkamp, T., and Müller, B., "Virtual histology of an entire mouse brain from formalin fixation to paraffin embedding. Part 1: Data acquisition, anatomical feature segmentation, global volume and density tracking," *J. Neurosci. Methods* **364**, 109354 (2021).

[3] Schnabel, J. A., Tanner, C., Castellano-Smith, A. D., Degenhard, A., Leach, M. O., Hose, D. R., Hill, D. L., and Hawkes, D. J., "Validation of nonrigid image registration using finite-element methods: application to breast MR images," *IEEE Trans. Med. Imag.* **22**(2), 238–247 (2003).

[4] Rohlfing, T., "Image similarity and tissue overlaps as surrogates for image registration accuracy: widely used but unreliable," *IEEE Trans. Med. Imag.* **31**(2), 153–163 (2011).

[5] Pluim, J. P., Muenzing, S. E., Eppenhof, K. A., and Murphy, K., "The truth is hard to make: Validation of medical image registration," in [*Int. Conference on Pattern Recognition*], 2294–2300, IEEE (2016).

[6] Rodgers, G., Schulz, G., Kuo, W., Scheel, M., Kurtcuoglu, V., Weitkamp, T., Müller, B., and Tanner, C., "Non-rigid registration to determine strain fields during mouse brain fixation and embedding," in [*Bioinspiration, Biomimetics, and Bioreplication XI*], **11586**, 55–64, SPIE (2021).

[7] Rodgers, G., Sigron, G. R., Tanner, C., Hieber, S. E., Beckmann, F., Schulz, G., Scherberich, A., Jaquiéry, C., Kunz, C., and Müller, B., "Combining high-resolution hard X-ray tomography and histology for stem cell-mediated distraction osteogenesis," *Appl. Sci.* **12**(12), 6286 (2022).

[8] Haskins, G., Kruger, U., and Yan, P., "Deep learning in medical image registration: A survey," *Mach. Vis. Appl.* **31**(1), 1–18 (2020).

[9] Jiang, X., Ma, J., Xiao, G., Shao, Z., and Guo, X., "A review of multimodal image matching: Methods and applications," *Inf. Fusion* **73**, 22–71 (2021).

[10] Chicherova, N., Hieber, S., Khimchenko, A., Bikis, C., Mueller, B., and Cattin, P., "Automatic deformable registration of histological slides to μCT volume data," *J. Microsc.* **271**(1), 49–61 (2018).

[11] Ammann, R., Tanner, C., Schulz, G., Osmani, B., Nalabothu, P., Töpper, T., and Müller, B., "Three-dimensional analysis of aligner gaps and thickness distributions, using hard X-ray tomography with micrometer resolution," *J. Med. Imaging* **9**(3), 031509 (2022).

[12] Izquierdo, A., Tanner, C., Schulz, G., von Jackowski, J. A., Rodgers, G., Deyhle, H., and Müller, B., "Three-dimensional imaging of human teeth - an in vitro study of caries detection using micro computed tomography," in [*Developments in X-Ray Tomography*], **12242-60**, SPIE (2022).

[13] Weitkamp, T., Scheel, M., Giorgetta, J., Joyet, V., Roux, V. L., Cauchon, G., Moreno, T., Polack, F., Thompson, A., and Samama, J., "The tomography beamline ANATOMIX at Synchrotron SOLEIL," *J. Phys. Conf. Ser.* **849**, 012037 (2017).

[14] Desjardins, D., Carcy, A., Giorgetta, J., Menneglier, C., Scheel, M., and Weitkamp, T., "Design of indirect X-ray detectors for tomography on the ANATOMIX beamline," in [*Mechanical Engineering Design of Synchrotron Radiation Equipment and Instrumentation*], (10), 355–357, JACoW Publishing (2018).

[15] Rodgers, G., Schulz, G., Deyhle, H., Kuo, W., Rau, C., Weitkamp, T., and Müller, B., "Optimizing contrast and spatial resolution in hard X-ray tomography of medically relevant tissues," *Appl. Phys. Lett.* **116**(2), 023702 (2020).

[16] Beckmann, F., Herzen, J., Haibel, A., Müller, B., and Schreyer, A., "High density resolution in synchrotron-radiation-based attenuation-contrast microtomography," in [*Developments in X-Ray Tomography*], **7078**, 410–422, SPIE (2008).

[17] Thurner, P., Beckmann, F., and Müller, B., "An optimization procedure for spatial and density resolution in hard X-ray micro-computed tomography," *Nucl. Instrum. Methods Phys. Res. B* **225**(4), 599–603 (2004).

[18] Klein, S., Staring, M., Murphy, K., Viergever, M. A., and Pluim, J. P. W., "elastix: A toolbox for intensity-based medical image registration," *IEEE Trans. Med. Imag.* **29**(1), 196–205 (2010).

[19] Shamonin, D., Bron, E., Lelieveldt, B., Smits, M., Klein, S., and Staring, M., "Fast parallel image registration on CPU and GPU for diagnostic classification of Alzheimer's disease," *Front. Neuroinform.* **7**, 50 (2014).

[20] Rodgers, G., Schulz, G., Kuo, W., Scheel, M., Kurtcuoglu, V., Weitkamp, T., Müller, B., and Tanner, C., "Non-rigid registration to determine strain fields during mouse brain fixation and embedding," in [*Bioinspiration, Biomimetics, and Bioreplication XI*], **11586**, 55–64, SPIE (2021).

[21] Rodgers, G., Tanner, C., Schulz, G., Migga, A., Kuo, W., Bikis, C., Scheel, M., Kurtcuoglu, V., Weitkamp, T., and Müller, B., "Virtual histology of an entire mouse brain from formalin fixation to paraffin embedding. Part 2: Volumetric strain fields and local contrast changes," *J Neurosci Meth* **365**, 109385 (2022).

[22] Rueckert, D., Sonoda, L. I., Hayes, C., Hill, D. L., Leach, M. O., and Hawkes, D. J., "Nonrigid registration using free-form deformations: Application to breast MR images," *IEEE Trans. Med. Imag.* **18**(8), 712–721 (1999).

[23] Maes, F., Collignon, A., Vandermeulen, D., Marchal, G., and Suetens, P., "Multimodality image registration by maximization of mutual information," *IEEE Trans. Med. Imag.* **16**(2), 187–198 (1997).

[24] Viola, P. and Wells III, W. M., "Alignment by maximization of mutual information," *Int. J. Comp. Vis.* **24**(2), 137–154 (1997).

[25] Mattes, D., Haynor, D. R., Vesselle, H., Lewellen, T. K., and Eubank, W., "PET-CT image registration in the chest using free-form deformations," *IEEE Trans. Med. Imag.* **22**(1), 120–128 (2003).

[26] Hansen, P. C., "The L-curve and its use in the numerical treatment of inverse problems," in [*Computational Inverse Problems in Electrocardiology*], 119–142, WIT Press (2000).

[27] Vescovi, R., Du, M., Andrade, V. d., Scullin, W., Gürsoy, D., and Jacobsen, C., "Tomosaic: Efficient acquisition and reconstruction of teravoxel tomography data using limited-size synchrotron X-ray beams," *J. Synchrotron Radiat.* **25**(5), 1478–1489 (2018).

[28] Miettinen, A., Oikonomidis, I. V., Bonnin, A., and Stampanoni, M., "NRStitcher: Non-rigid stitching of terapixel-scale volumetric images," *Bioinformatics* **35**, 5290–5297 (05 2019).

[29] Tanner, C., Rodgers, G., Schulz, G., Osterwalder, M., Mani-Caplazi, G., Hotz, G., Scheel, M., Weitkamp, T., and Müller, B., "Extended-field synchrotron microtomography for non-destructive analysis of incremental lines in archeological human teeth cementum," in [*Developments in X-Ray Tomography XIII*], **11840**, 182–191, SPIE (2021).

[30] Yushkevich, P. A., Gao, Y., and Gerig, G., "ITK-SNAP: An interactive tool for semi-automatic segmentation of multi-modality biomedical images," in [*Int. Conf. of the IEEE Engineering in Medicine and Biology Society*], 3342–3345, IEEE (2016).

[31] Otsu, N., "A threshold selection method from gray-level histograms," *IEEE Trans. Syst. Man Cybern.* **9**(1), 62–66 (1979).

[32] Schenk, A., Prause, G., and Peitgen, H.-O., "Efficient semiautomatic segmentation of 3D objects in medical images," in [*Int. Conf. on Medical Image Computing and Computer-Assisted Intervention*], 186–195, Springer (2000).